Investigation of Spectro-Angular Albedo of Diffuse, Glossy, and Specular Surfaces for Enhanced Photovoltaic Output

Capstone Project

University College Twente (ATLAS)

Author:
Jelle Westerhof

Supervisors:
Shweta Pal
Dr. Rebecca Saive
Dr. Ir. Fokko Jan Dijksterhuis

June 23, 2021

UNIVERSITY OF TWENTE.

Abstract

The spectral and angular nature of the ground reflectance, i.e., albedo, plays a key role in enhancing bifacial photovoltaic output. A general framework to describe any reflector assumes that the total reflection, while being dependent on the surface roughness, can be expressed as a linear combination of the three types of reflection, i.e, diffuse, glossy, and specular. The surface roughness and its influence on the reflection is modelled using three terms: the Fresnel term, a microfacet distribution and a shadow-masking function. For perfectly diffuse or Lambertian reflection, all light is scattered equally over the hemisphere. For specular reflection, the light is reflected fully over the angle of incidence and for glossy reflection, the light is reflected in a lobe around the angle of incidence. Such an approach using a linear combination of the three types of reflection can enable a more fundamental understanding of the reflector and help in enhancing albedo-dependent photovoltaic yield. Yet important parameters for this computational model are missing.

This thesis experimentally provides the necessary parameters using various reflection models. For the measurements, an existing experimental set-up has been optimized and the spectro-angular albedo of a Lambertian surface, paper, photo paper, and aluminium mirror was measured. It is expected that each of these surfaces are extremes of one of the types of reflection: Lambertian and paper are expected to be diffuse, mirror is expected to be specular, and photo paper is expected to be glossy. Diffuse reflection was observed for the Lambertian surface, paper and photo paper and this was modelled with a cosine fit. Glossy behaviour was observed for photo paper as well as slightly for the normal paper and Ward's reflection model was used to fit glossy/specular reflection onto the paper, photo paper and mirror sample. For the Lambertian reflector it was concluded that all the light was reflected diffusely, and for the mirror, all the light was reflected specularly. The photo paper was an intermediate case where both glossy as well as diffuse reflection was observed, and paper was mostly diffusive but there was also some glossy reflection, especially at larger angles of incidences, due to the Fresnel term.

Keywords: Spectro-angular albedo, bifacial photovoltaics, PV output.

Acknowledgments

First and foremost, I would like to thank the entire Saive Research group for the great working environment in which everyone works together in a very positive way. I felt very welcome in the group. Furthermore I am very grateful to Shweta for her great support (and food) during this project and for always being available to help out with anything, to Rebecca for asking the right questions that made me realize my mistakes, for always being available for meetings even at short notice, and for pushing me to do the normalisation, to Fokko Jan for helping with the procedural aspects and for proposing new ideas that I had not thought of before, to Geert for being available to have discussions about certain things such as the set-up that was designed, and lastly to Jarco for taking good care of me during the busiest times.

In addition, I would like to thank the whole of IMS for being very open and welcoming and for the interesting talks during the coffee and lunch breaks and the fun game nights.

Abbreviations and Nomenclature

η Efficiency

λ Wavelength

ϕ_i Incident azimuth angle

ϕ_r Reflected azimuth angle

σ Root mean square slope

θ_i Incident zenith angle

θ_r Reflected zenith angle

D Microfacet distribution

F Fresnel term

G Shadowing-masking function

I_{sc} Short-circuit current

J_{sc} Short circuit current density

P_{max} Maximum power output

V_{oc} Open-circuit Voltage

BRDF Bidirectional reflectance distribution function

EQE External Quantum Efficiency

FF Fill Factor

LACE Levelized Avoided Cost of Electricity

LCOE Levelized Cost of Electricity

NA Numerical Aperture

PERC Passivated Emitter and Rear Cell

PV Photovoltaics

Contents

1   Introduction

The global energy demand has been growing almost consistently since at least 1980, with 2020 being an exception due to the COVID-19 pandemic (IEA, 2020a,b). It is, however, expected that the need for electricity will keep growing in the coming decades (Taibi et al., 2018). The traditional burning of fossil fuels is accelerating climate change and global warming, causing a need for renewable energy sources (Sampaio and González, 2017). In the coming years, at least 60% of the electricity needs to come from renewable sources to realize a future based on sustainable energy (Taibi et al., 2018). Photovoltaic (PV) cells are amongst the primary contenders (EIA, 2020). PV cells are cells that can generate electricity from sunlight. A set of encapsulated PV cells, connected either in series or in parallel, constitutes a module. The cost of these modules is now ten times lower than in 2000. However, this decrease has converged over the last few years causing the increase of the yield of the modules to become a top priority (Kopecek and Libal, 2018; Feldman and Margolis, 2020).

One of the ways to increase the yield of solar cells, while keeping the costs low, is the use of bifacial cells. In contrast to their counterpart (the monofacial cells), these bifacial modules can also accept scattered light from the rear side. A schematic comparison between monofacial and bifacial modules is given in figure 1.
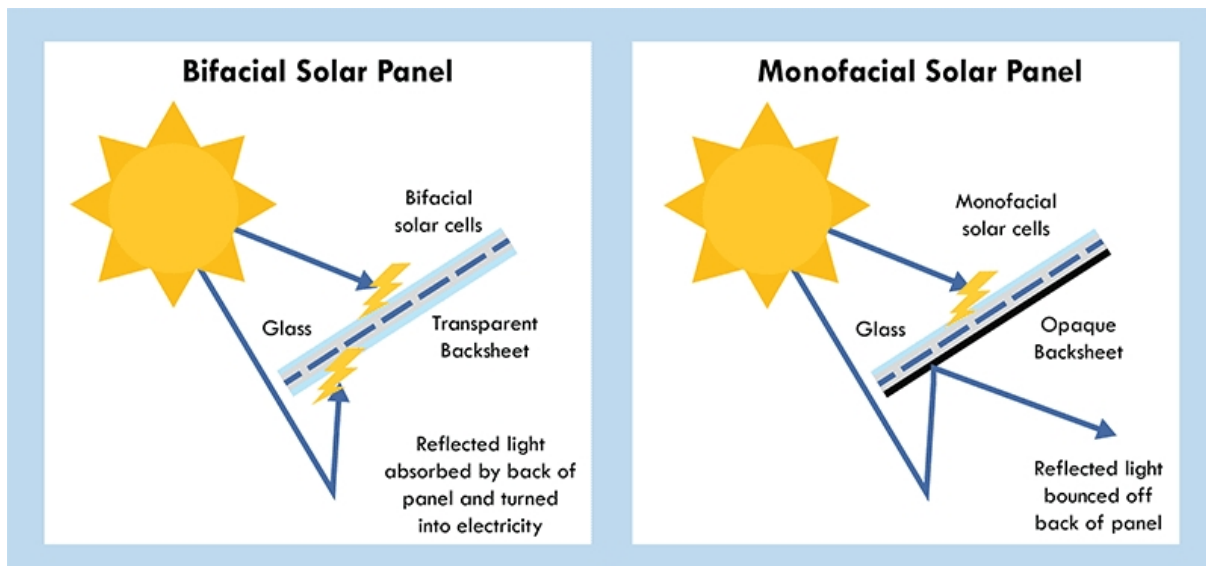

Figure 1: *A schematic comparison between monofacial and bifacial solar cells. Bifacial cells can, in addition to the light that is captured at the front of the panel, also collect light at the back of the panel, while monofacial cells can not. From Gambone (2020).*

In the 1980s Cuevas et al. (1982) found that these bifacial cells have (under ideal circumstances) the potential to produce 50% more electricity than its monofacial counterpart. However, only recently manufacturers actually started to produce and sell these cells (Russell et al., 2017). This is mainly due to the fact that the thin glass backsheets from the modules have dropped in price enough for them to become financially attractive (Kopecek and Libal, 2018). Cells with passivated rear sides, such as Passivated Emitter and Rear Cell modules (PERC), are expected to maintain dominance throughout the upcoming decade (VDMA, 2020). These cells can in principle also be used for bifacial light capturing, if the modules containing these cells are designed accordingly.

The output of the rear of the module depends, amongst others, on the reflectance of the ground surface i.e., albedo (Yusufoglu et al., 2015; Katsaounis et al., 2019; Phillips et al., 2020; Pal and Saive, 2020). The albedo of a surface is defined as the ratio of the irradiance of the reflected light to that of the incoming light. This reflectance is, generally, a function of wavelength and viewing angle. We refer to it as spectro-angular albedo or spectro-angular reflectance. Accounting for the spectral and angular dependence of the albedo is an important ongoing research into what extend albedo influences the PV output and how it can be used to increase the yield.

1.1 A cost comparison

The power enhancement results of bifacial modules are promising, but bifacial modules are inherently more expensive and, depending on the configuration, monofacial cells might be more cost-effective (Rodríguez-Gallegos et al., 2018). As market penetration of an energy resource is cost-driven (Paidipati et al., 2008), bifacial PV cells need to reach a financially competitive position before they can be widely implemented. The Levelized Avoided Cost of Electricity (LACE) and the Levelized Cost of Electricity (LCOE) are globally recognized economic metrices used to assess the financial viability of an energy source (VDMA, 2020).

The LCOE is defined as the total cost of an electricity source over its lifetime divided by the total power output over its lifetime and the LACE takes into account the daily and seasonal variations in demand (EIA, 2020). In addition to this, LACE takes into account the current generation of electricity by comparing it with the prospective generation. PV sources that replace fossil fuels will thus have a different LACE than PV sources replacing another source. Electricity sources are economically viable if the costs that are avoided by the implementation of the energy source (LACE) are higher than the costs of the energy source itself (LCOE). Figure 2 shows the LACE/LCOE relations for different types of energy sources and among these, solar photovoltaic is the most economically competitive (EIA, 2020). One of the ways to further reduce the LCOE of PV modules is to increase the yield, which can be done by the use of bifacial modules (Libal et al., 2017; Fertig et al., 2016).

It has been found that for lattitudes above $40°$ bifacial modules tend to be more cost-effective than the monofacial modules. For lower lattitudes an optimized albedo is required for bifacial modules to outperform monofacial ones (Rodríguez-Gallegos et al., 2018; Ito and Gerritsen, 2016). However, a comprehensive research on the effect of the spectro-angular albedo on these bifacial modules is lacking (Pal and Saive, 2020), causing the output of the bifacial cells to be unpredictable (Katsaounis et al., 2019; Sun et al., 2018). To aid this, Pal and Saive (2020) developed a reverse ray-tracing software to calculate the albedo-dependent output of a bifacial module for different classes of reflectors. This computational model uses the principle that the reflectance of any surface, which is dependent on the roughness of the surface, is given as a linear combination of reflectance of diffuse, glossy, and specular surfaces:

$$f_{\text{total}} = k_d \cdot f_{\text{diffuse}} + k_g \cdot f_{\text{glossy}} + k_s \cdot f_{\text{specular}}, \tag{1}$$

in which each function (f) describes the reflection class and k are parameters describing the amount of light that is reflected following that class. The coefficients k_d, k_g, and k_s must be empirically derived. To do this, I optimised an existing experimental set-up and I measured the spectro-angular albedo of paper, photo paper, a Lambertian reflector and a mirror. It is expected that each of these surfaces are extremes of one of the types of reflection: Lambertian and paper are expected to be diffuse, mirror is expected to be specular, and photo paper is expected to be glossy. The measured reflectivity was
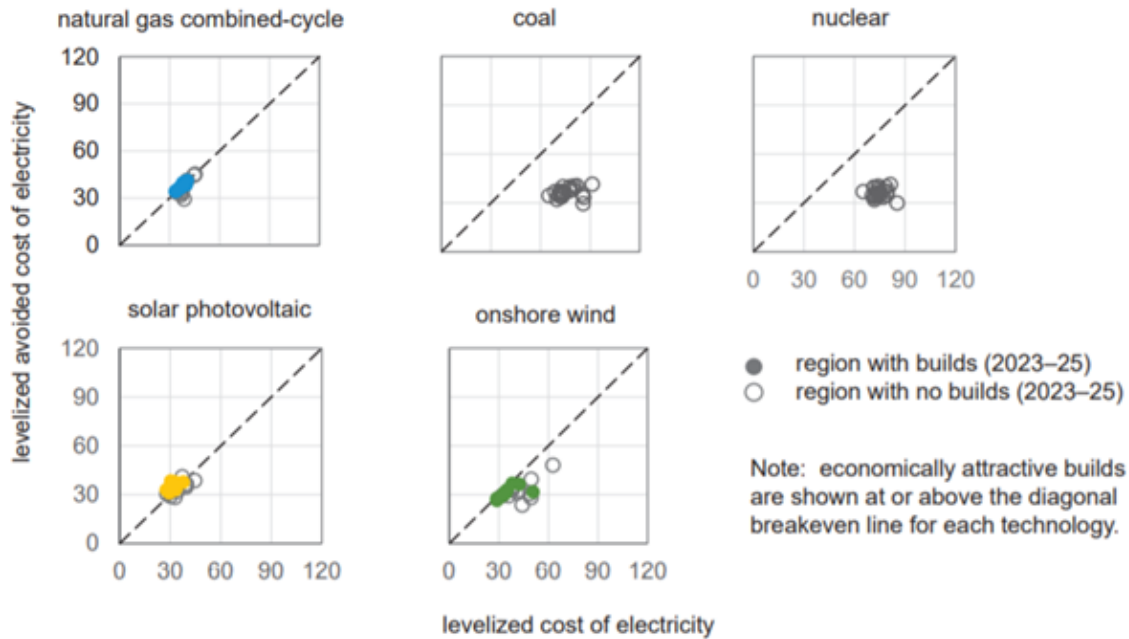
Figure 2: *An LACE/LCOE comparison for different types of energy sources. From EIA (2020).*

analysed by me and can also be used to assess the merit of the computationally simulated results of the ray-tracing software. Such a computational and experimental approach can enable a more general framework to understand the impact of albedo on PV yield fundamentally and help with the further improvement of it.

Chapter 2 discusses the working of solar cells and draws comparisons between monofacial and bifacial cells, describes the physics of surface reflection, and details the main classes of reflectors, namely, diffuse, glossy and specular.

In chapter 3 the experimental set-up and its components are detailed. In addition to this, the section describes the used methodology and details the error in the experiments.

Chapter 4 gives all the results from the measurements on the four different samples and fits are made to match these data points. In the Conclusion & Discussion (chapter 5) these results are then further discussed and the limitations of this study are given. In addition to this, opportunities for further research into the possibilities for yield enhancement of bifacial PV modules are given.

2 Theoretical Framework

Bifacial cells offer an economically competitive way to harness the sunlight renewably. To discuss the merit of these cells, a basic understanding of solar cells is needed. The chapter is divided as follows: section 2.1 discusses the working of solar cells and draws comparisons between monofacial and bifacial cells . Section 2.2 describes the physics of surface reflection and details the main classes of reflectors, namely, specular, diffuse, and glossy.

2.1 Solar cells

In solar cells, the electricity is generated by exploiting certain properties of a material (often silicon) to induce the photoelectric effect (Nelson, 2003). The energy of light (photons) is used to excite the electrons that are bound to the material to higher energy levels. These electrons are then driven through an electrical circuit (Nelson, 2003). Generally speaking, there are four important quantities that describe the performance of a PV solar cell: the open-circuit voltage (V_{oc}), the short-circuit current (I_{sc}), the fill factor (FF), and the efficiency (η). The generated voltage when neither of the terminals of the solar cell are connected, is called the open-circuit voltage, and this is the maximum voltage achievable for the system. The current that is flowing through the circuit without a load is called the short-circuit current, and this is the maximum current achievable for the system. The Fill Factor is defined as the maximum power output (P_{max}) of the solar cell divided by the short-circuit current density (J_{sc}) and the open-circuit voltage (Nelson, 2003):

$$\mathrm{FF} = \frac{P_{\mathrm{max}}}{J_{\mathrm{sc}} V_{\mathrm{oc}}}.$$

For solar cells, J_{sc} is the short-current density under normal illumination conditions (AM 1.5) (Bisquert, 2008). J_{sc} is dependent on the cell's External Quantum Efficiency (EQE), which is a metric defining the probability of an incident photon being converted into a electron-hole pair that can flow through the circuit of the solar cell. Finally, η is defined as the maximum power as the fraction of the incident power density (Nelson, 2003). Having defined these quantities, it now becomes possible to make comparisons between the performance of standard monofacial modules and the bifacial modules.

2.1.1 Bifacial cells

Bifacial cells are cells that can accept light from both sides, front and rear, of the cell to boost PV output. These modules are different from the typical monofacial modules that can often be seen outside such as on the rooftops of houses as these monofacial modules do not accept incident light from the back of the panel. A comparison in the cross section between a typical monofacial and standard bifacial module is shown in figure 3.

Using the parameters defined in the previous section, bifacial solar cells mainly outperform their monofacial counterpart with respect to the J_{sc} as more current is generated under the same illumination conditions. Through similar reasoning, the efficiency η is also higher for bifacial solar cells as also more power is generated under the same illumination conditions.

The optimum height and tilt of a bifacial module tends to be different from its monofacial counterpart. Because monofacial cells do not capture light from the back side, they can also be placed close to a surface such as a roof. On the other hand, bifacial modules perform better when they are tilted at an angle so that more light can be accepted from the rear side (Porter, 2019; Solar Magazine, 2020)
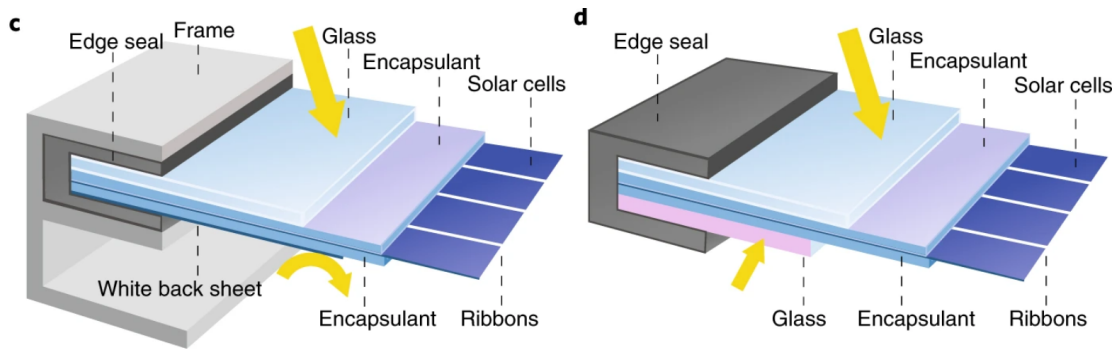
Figure 3: *Cross-sections from both a monofacial module (left) and a bifacial module (right). The main difference is the opaque white back sheet for the monofacial module and the thin glass sheet for the bifacial module. From Kopecek and Libal (2018).*

or when they are raised higher from the ground to avoid self-shading. Residential use of bifacial solar cells on rooftops is thus not as obvious. However, there are many innovative examples of how bifacial solar cells can still be used, not only on large industrial solar plants but also in space on satellites or as sunshade in front of the window, as the roof of a carport or slightly separated from the walls of an office building with a white diffuse reflector as reflecting surface (Hezel, 2003). Bifacial cells can also be used in combination with light trapping techniques such as luminescent solar concentrators or holographic optical elements for further enhancement of PV output (Einhaus and Saive, 2020; Xu et al., 2020; Pelaez et al., 2018). In combination with a 1-axis tracker system, bifacial modules are reported to outperform a monofacial fixed reference by 24% even with a non-ideal albedo of 30% (Dullweber et al., 2018).

2.2   Reflection

One of the main reasons that bifacial PV modules are not as widespread yet is the unpredictability of the output due to the difficulty in quantifying the rear irradiance (Katsaounis et al., 2019; Sun et al., 2018), which depends on the albedo properties of the ground reflector. It is expected that the total reflection of incident light on the surface can be a linear combination of the three main types of reflection, namely diffuse, specular, and glossy (see figure 4 and equation (1)). Each of these types will be discussed in detail in the upcoming sections. Before that, first a rigorous framework to model reflection and sample surfaces will be given.

Nicodemus (1965) was the first to introduce the bidirectional reflectance distribution function (BRDF) as a way to model the reflection of light from a surface. This five-dimensional function makes use of the Helmholtz reciprocity and can describe how light reflects from a surface (see figure 5). The Helmholtz reciprocity principle means that the angle of incidence and angle of reflection can be interchanged without changing the reflection properties. The BRDF is dependent on the incident angle (both azimuth and zenith angles (ϕ_i & θ_i respectively)), the angle of reflection (again both azimuth and zenith angles (ϕ_r & θ_r, respectively)) and the wavelength of the light (λ). In this thesis, the azimuth angle is defined as the angle on the surface of the sample and the zenith angle is defined as the angle with respect to the surface normal. When performing measurements on reflection, these five quantities need to be known to be able to describe reflection and they should be included when performing reflection measurements. However, most surfaces are isotropic, meaning that their material properties are independent of direction or rotation. If this is the case, azimuth symmetry exists and
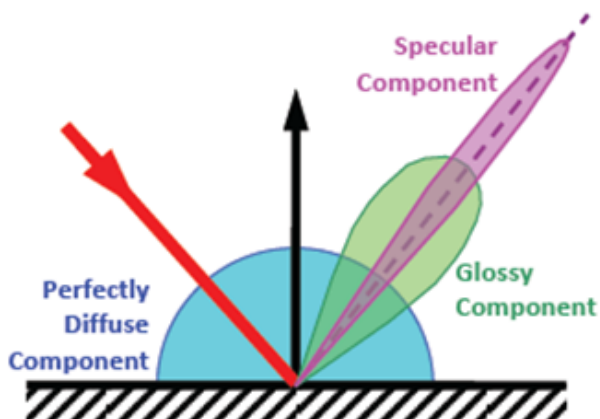
Figure 4: *The three different types of reflection (specular, diffuse, and glossy) when a light source is incident on a surface are shown. Usually the reflective surface lies somewhere between these three extremes. From Viral International (2014).*

the function becomes independent of both (incident and reflected) azimuth angles (Nicodemus, 1965). In present study, it is assumed that all used samples are isotropic and thus azimuthal symmetry is used.

Nicodemus (1965) found that the total directional reflectance for a collimated beam that is incident on an opaque surface is the ratio between the reflected irradiance and the incident irradiance. It is described as the radiance $(dL(\theta_r, \phi_r))$ that is reflected from a sample as a fraction of the incoming radiance $(dE(\theta_i, \phi_i))$ by the following equation (Wang et al., 2013):

$$f_r(\theta_i, \phi_i; \theta_r, \phi_r) = \frac{dL(\theta_r, \phi_r)}{dE(\theta_i, \phi_i)}. \tag{2}$$

2.2.1 Surface roughness

The way light reflects from a surface is largely dependent on the surface roughness, i.e. features on the surface. This subsection details principles used to model the structure of a sample.

The Fresnel equation (for unpolarized irradiance) (equation (3)) defines the reflectance of a surface as a function of wavelength and θ_i and θ_r. The Fresnel term F can be modeled the following way (Walter et al., 2007):

$$F(\mathbf{i},\mathbf{m}) = \frac{1}{2} \frac{(g-c)^2}{(g+c)^2} \left(1 + \frac{c(g+c)-1)^2}{c(g-c)+1)^2} \right), \tag{3}$$

$$\text{with } g = \sqrt{\frac{n_t^2}{n_i^2} - 1 + c^2}, \text{ and } c = |\mathbf{i} \cdot \mathbf{m}|.$$

In this equation, n_t and n_i are the refractive index of the sample and the transmitting medium (usually air), $\mathbf{i}$ is a vector describing the incoming rays, and $\mathbf{m}$ is the normal of the microfacet surface (see the
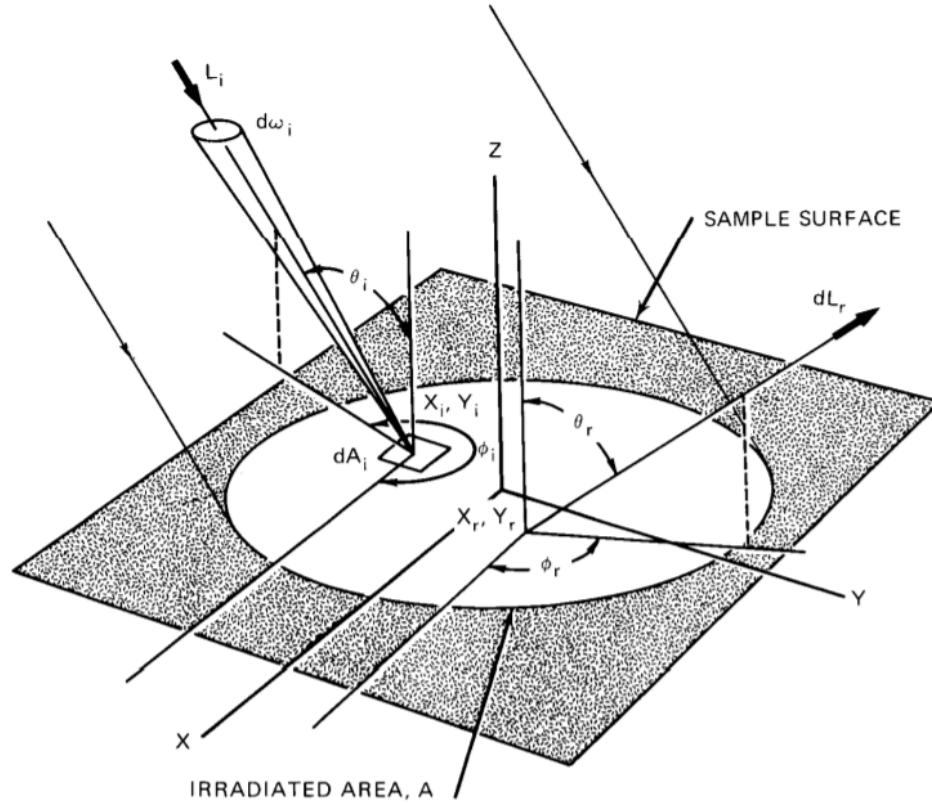
Figure 5: *A schematic drawing of how the BRDF can be used to calculate the reflecting irradiance to different directions. From Nicodemus et al. (1992).*

next section). The Fresnel term is increasingly large if there is a large difference between the angle of incidence and the surface normal, thus causing more light to be specularly reflected (see section 2.2.2).

The Fresnel term is dependent on the normal of the surface. The Beckmann distribution (see equation (4)) can be used to model this normal by modelling the surface as a collection of microfacets (see figure 6) (Cook and Torrance, 1981). In this distribution, α is the angle between the surface normal and the normal of the microfacets, and σ_α is the root mean square slope of the facets.

The GGX distribution (equation (5)) on the other hand, while being similar, has stronger tails than the Beckmann distribution and better models the shadowing.

$$D(\alpha) = \frac{1}{4\sigma_\alpha^2 \cos^4(\alpha)} e^{-(\tan(\alpha)/\sigma_\alpha)^2}. \tag{4}$$

$$D(\alpha) = \frac{\sigma_g^2}{\pi \cos^4(\alpha)(\sigma_g^2 + \tan^2(\theta_v))^2}. \tag{5}$$

Based on these distributions of microfacets, some of the irradiance incident on the surface will also be masked or shadowed as depicted in figure 6. The influence of this effect is described in the shadowing-

masking function (G). As the shadowing-masking function also depends on the configuration of microfacets in the Beckmann distribution, it is often impossible to find an exact expression for this function (Walter et al., 2007).
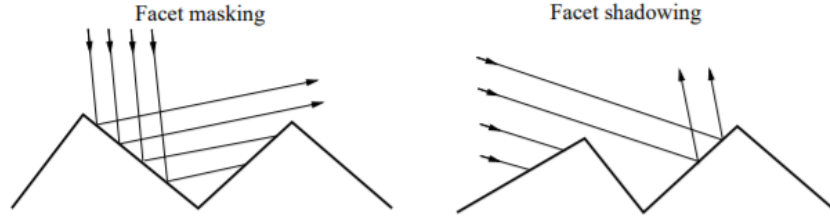

Figure 6: *A schematic drawing of how the surface roughness causes facet masking and facet shadowing. From Love (1997)*

.

Using these three functions (F, D, G) and the required parameters (θ_i, θ_r, ϕ_i, ϕ_r, λ), the different types of reflection (specular, diffuse, and glossy) that are given in the sections ahead can described.

2.2.2 Specular

If the surface is smooth, i.e. irregularities are very small compared to the wavelength of the incident light, specular or mirrorlike reflection occurs (Hecht, 2017). For specular reflection, each light ray is reflected over the surface normal in the opposite direction. Mathematically this can be modelled the following way (Love, 1997):

$$f_{\text{specular}}(\theta_i, \phi_i; \theta_r, \phi_r; \lambda) = \frac{\delta(\cos(\theta_i)\cos(\theta_r))}{\cos(\theta_i)} \delta(\phi_i - (\phi_r + \pi)), \tag{6}$$

in which δ is the Dirac delta distribution: a distribution that is zero everywhere except for at 0 and its integral is 1. A good example of a specular surface is a mirror.

2.2.3 Diffuse

If the surface irregularities are very large compared to the wavelength of the incident light, diffuse reflection occurs (Hecht, 2017). Perfectly diffuse, or Lambertian, surfaces have equal reflectance in all directions, this is called Lambert's law (Lambert, 1760). Diffuse reflection can be mathematically modelled in the following way:

$$f_{\text{diffuse}} = \frac{1}{\pi}. \tag{7}$$

A good example of a diffuse surface is normal paper. However, special Lambertian surfaces, such as spectralon, also exist (Georgiev and Butler, 2007). Spectralon is a white diffuse material with optimal reflection properties over a large wavelength bandwidth. It has the highest known diffusive reflectance of any material (Georgiev and Butler, 2007).

2.2.4 Glossy

Glossy reflection is the intermediate case between specular and diffuse. There is maximum reflection along the $\theta_r = \theta_i$ direction with diffuse reflection at the other angles. Glossy reflection can be modelled using the following equation (Cook and Torrance, 1981):

$$f_{\text{glossy}}(\theta_i, \phi_i; \theta_r, \phi_r; \lambda) = \frac{DGF}{\pi \cos \theta_i \cos \theta_r}, \tag{8}$$

in which D, G, and F are the previously defined functions for reflection and surface roughness. A good example of a glossy surface is photo paper.

2.2.5 Ward's reflection model

Equation (8) is relatively complex and defining the three functions (D, G, and F) is not always trivial. The model proposed by Ward (1992) (equation (9)) does not take into account the Fresnel term or the shadowing-masking function, but does take into account the conservation of energy over the hemisphere. Even though it is not as comprehensive as other models, it still provides an accurate model for light reflection (see for example Mardaljevic (1995)).

$$f(\theta_i, \phi_i; \theta_r, \phi_r; \lambda) = \frac{\rho_d}{\pi} + \rho_s \frac{1}{\sqrt{\cos(\theta_i)\cos(\theta_r)}} \frac{\exp(-\tan^2(\delta)/\sigma^2)}{4\pi\sigma^2}, \tag{9}$$

in which σ is again the rms slope, δ is the half angle defined as $\delta = \theta_r + \theta_i$, and ρ_d and ρ_s are fitting parameters for diffuse and specular reflectance and $\rho_d + \rho_s \leq 1$. This function has to be corrected by a factor $\cos(\theta_r)$ to account that a larger area is seen by the fibre when viewing from an angle θ_r (Georgiev and Butler, 2007):

$$f(\theta_i, \phi_i; \theta_r, \phi_r; \lambda) = \left(\frac{\rho_d}{\pi} + \rho_s \frac{1}{\sqrt{\cos(\theta_i)\cos(\theta_r)}} \frac{\exp(-\tan^2(\delta)/\sigma^2)}{4\pi\sigma^2} \right) \cos(\theta_r). \tag{10}$$

The above special classes of materials (see section 2.2.2-2.2.4) can be used to describe the nature of a ground-reflector. This will be crucial in calculating the irradiance on the rear side of a bifacial module, thereby, helping in calculating the output due to rear side irradiance. Furthermore, such an understanding will also help in assessing already existing reflectors such as grass, sand etc., along with novel reflectors like luminescent solar concentrators and metamaterials.

3   Experimental Set-up

Spectral measurements of reflected irradiance from various angles is key in fully understanding the reflection properties of various surfaces. This chapter details an experimental set-up that can be used to perform measurements to acquire the required quantities.

The set-up and equipment used in this study consists of four main parts that are also depicted in figure 7: The white light fibre source (1) and the collimation part where this light source is collimated (2), the goniometer on which this spectrometer is placed to measure the reflected intensity for different angles on various samples (3), and the grating spectrometer (4). The parts are rigidly connected so that they cannot move with the respect to the other parts. Each part will be discussed in its own subsection ahead.
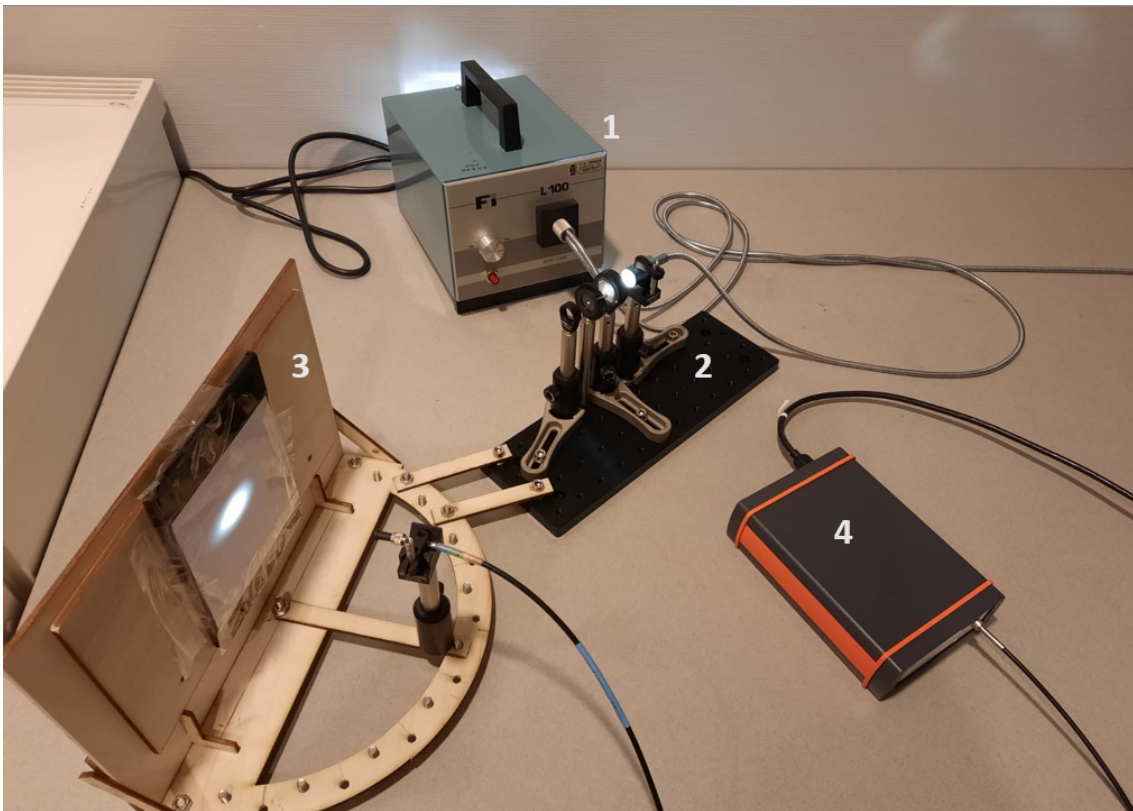

Figure 7: *A picture of the measurement set-up that is used to perform the experiments. This picture includes the white light fibre source (1), the collimation set-up (2), the goniometer (3) and the fibre spectrometer(4).*

3.1   The light source

The light source used is a Fiberoptic Heim FI L100 light source. The light is emitted via two separate fibres differing in beam diameter and divergence. The spectra, at maximum and minimum setting, of the fibre with bigger beam diameter (divergence-4°), and smaller beam diameter (divergence-undefined) are shown in figure 8. The data in this graph was obtained by Shweta Pal by pointing a cosine corrected calibrated spectrometer (wavelength range: [300-1100nm]) directly at the source before the collimation step. This data is gathered with a different spectrometer then the rest of the data as the

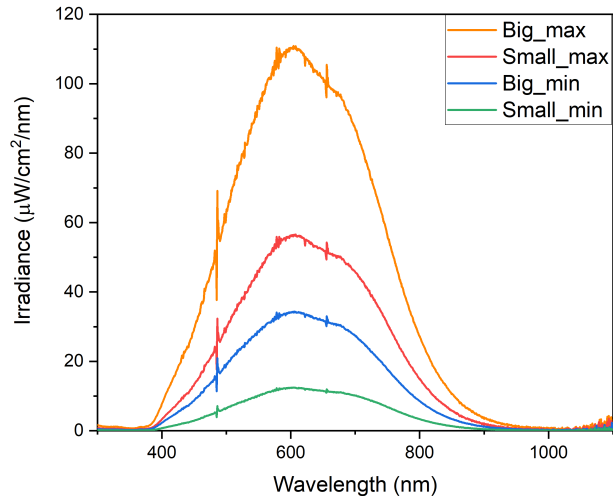spectrometer used here was under maintenance during the duration of this study.

Figure 8: *The spectra of the used white light fibre source. For both the small diverging and big slightly diverging fibre the spectra are shown for their minimum and maximum intensity*

3.2 The collimation set-up

For ideal illumination, the incoming beam must be collimated. Firstly, a collimated beam has a well defined beam path which can be used to illuminate a small part of the sample. Secondly, the spot size from the collimated beam is smaller than that of the uncollimated beam and more homogeneous. Both of these help when normalizing the data with respect to the incident irradiance.

A schematic drawing of the collimation part of the set-up can be found in figure 9 and a picture in figure 10. The lenses used in these experiments are UV-fused silica plano-convex lenses (range of 185 nm - 2.1 μm). These lenses are near best form for infinite conjugate applications which means that they can be used to focus collimated light sources or to collimate light sources from point sources. First, the diverging input is focused, using a plano-convex lens, at the aperture of a 0.08 mm wide irise. The pinhole then becomes a virtual point source which can be collimated by putting it at the focal length of the second lens with the planar side towards it. The set-up could also work if the lenses are flipped, but this configuration, with the planar side towards the pinhole, minimises chromatic aberrations.

3.3 The goniometer

A goniometer is an instrument used to measure the reflected intensity at various angles. The goniometer used here is an upgraded version of previously designed set-up for higher quality data. The new design was developed and realised with the help of Shweta Pal and Geert Heres using the CorelDraw 2018 software. A laser cutter has been used to cut the design out of 4 mm plywood. The file that was used for the lasercutter is given in Appendix A. The cut pieces were assembled and the final result of
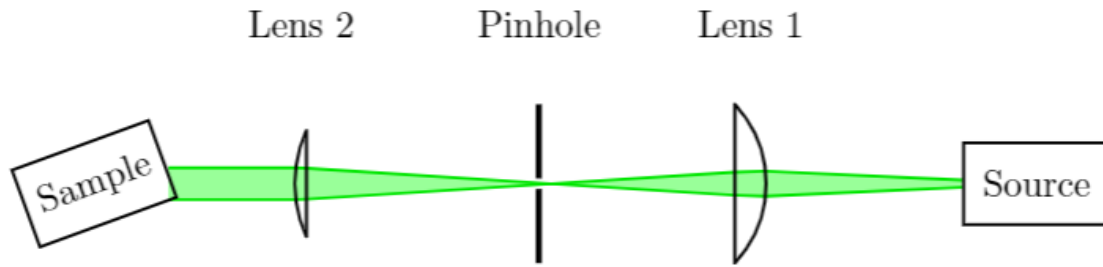
Figure 9: *A schematic drawing of the set-up that is used to collimate the white light fibre source.*

Figure 10: *A picture of the set-up that is used to collimate the white light fibre source.*

this assembly can be found in figure 11. A sample can be attached to the backplate of the goniometer and the fibre can then be placed at different angles to measure the reflected intensity. The angle of the goniometer with respect to the collimation set-up is variable to achieve different angles of incidence for the light source. Self-shading occurs when the fibre is placed at the same angle on the goniometer as the angle of incidence as the fibre then blocks the incoming light.

For all samples in this study azimuthal symmetry is assumed such that this 2D goniometer is sufficient to perform measurements.

3.4   The spectrometer

A grating spectrometer is an instrument that can measure the spectrum of incident light. Wavelengths of the incoming light are spatially separated, i.e., dispersed, using a grating, causing light of different wavelengths to constructively interfere at different spots. This interference occurs at a sensor, namely, a CCD or CMOS camera. Intensity at each pixel or location is measured, thus giving a spectral profile of the incident light.

The spectrometer used in these experiments is an AvaSpec-ULS2048CL-EVO. This spectrometer works
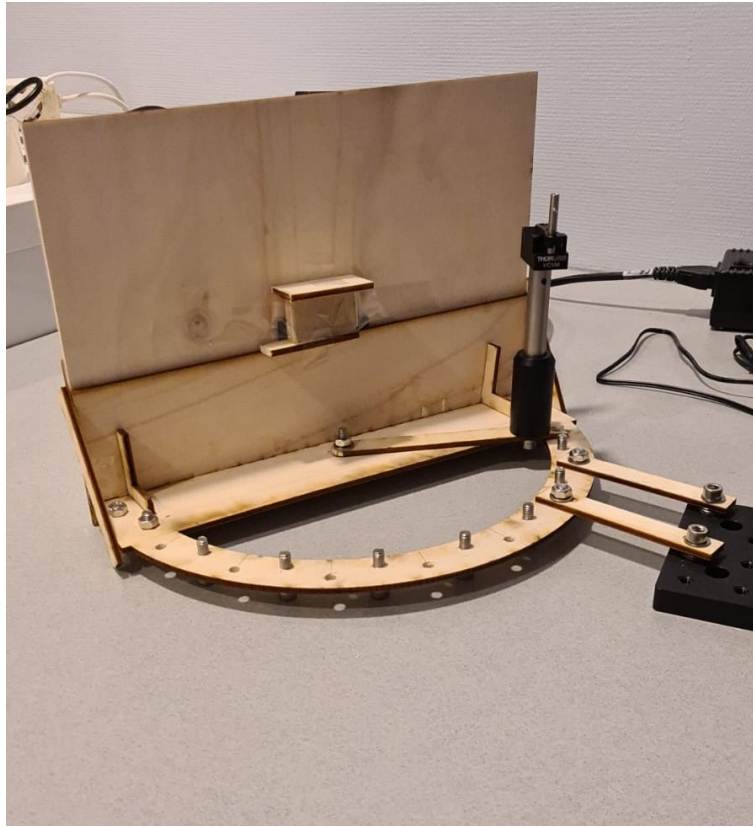
Figure 11: *A picture of the goniometer.*

in the 200-850nm range (UV-VIS range) and has a grating with 600 lines/mm. The intensity measured by the spectrometer has a maximum error of 1%. The fibre that is connected to this spectrometer is a StellarNet Fiber Optic Cable with a Numerical Aperture (NA) of 0.22 and a core diameter of 1000 μm. This gives the fibre an exceptance cone of 25.4°.

3.5 UV-VIS spectrometry

In addition to the measurements taken with the previously described set-up, measurements were also performed (by Shweta Pal) using a UV-VIS spectroscope. This spectroscope uses an integrating sphere (see figure 12) made of spectralon (perfectly diffuse high reflectivity material). This instrument gives the reflectance (relative to the spectralon) of samples for a large wavelength spectrum (300-1200 nm). However, due to the nature of the integrating sphere, the angular dependent reflectance can not be acquired from these measurements. The measurements performed on the UV-VIS spectrometer are independent of the measurements performed on the previously described set-up and they can be compared to check the validity of the measurements and to help with the normalisation. The error of the UV-VIS is 0.2%.

3.6 Methodology

For a higher signal-to-noise ratio the experiments were performed in a dark room. In addition to this, dark measurements are made by blocking the light source to account for stray light and irregularities. The data from these dark measurements are then subtracted from the measured signal to obtain clean
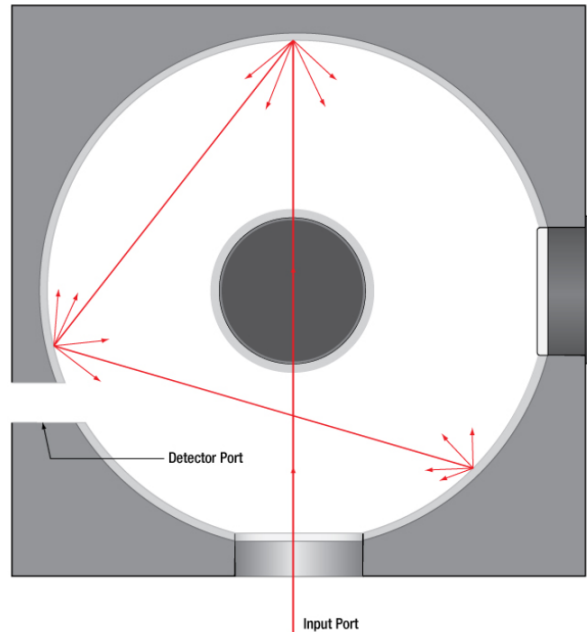
Figure 12: *A schematic drawing of an integrating sphere as also used in the UV-VIS spectroscope. From Thorlabs (2021).*

data.

During the measurements, the fibre is placed on the entire range of the goniometer with 10° step-size. At the places where the angle of reflection is approximately equal to the angle of incidence, instead 5° step-sizes are taken to ensure that glossy or specular reflection can be properly documented. After placing the fibre at the desired spot on the goniometer, the fibre is turned until a maximum in signal is found.

Measurements are performed on the samples that are expected to best describe the three cases of reflection: Paper and a Lambertian surface for diffuse reflection, photo paper for glossy reflection and a mirror for specular reflection.

3.7   Normalisation

To be able to compare the measurements with each other and also get the parameters from equation (1) for various materials, the data needs to be normalised. The first step in the normalisation process is the use of the integration time to go to counts per second. As the measured intensity (in counts) scales linearly with the integration time (see figure 13), a simple division by integration time is sufficient for this step.

In addition to this, measurements are only performed in 1 dimension on the goniometer (along the zenith (θ) angle). However, for diffuse reflection, the light is reflected in all directions, meaning that not all the light is measured during the measurements and that some of the light is also lost. Using the azimuth symmetry that was established in the Theoretical Framework, attempts can still be made to go from this 1D measurement to a 2D surface in which the reflected intensity is defined over the entire hemisphere. The following integral is used for this:
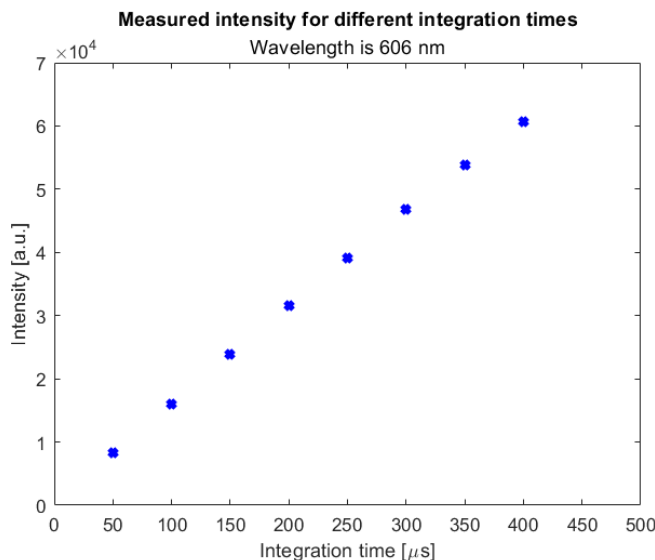
Figure 13: *Measured intensity depending on the integration time. A linear relation can be observed.*

$$f_{\text{total}} = \int_0^{2\pi} \int_0^{\frac{\pi}{2}} \frac{f_r(\theta_r, \phi_r)}{A} \sin(\theta_r) \mathrm{d}\theta_r \mathrm{d}\phi_r, \tag{11}$$

where f_{total} is the approximated total reflected irradiance over the hemisphere, f_r is the measured reflected irradiance, and A is the cross-sectional area of the fibre of the spectrometer.

3.8 Measuring error

While performing measurements using the goniometer set-up as described above, various factors influence the error of said measurement. The total relative error can be expressed as follows:

$$\epsilon_{\text{total}}^2 = \epsilon_{\text{Goniometer}}^2 + \epsilon_{\text{Source}}^2 + \epsilon_{\text{Spectrometer}}^2 + \epsilon_{\text{Human}}^2, \tag{12}$$

In which each error subscript describes what influences the error.

When attaching a sample to the goniometer, the sample can be of center or tilted with respect to the goniometer surface normal. Based on other literature (for example Wang et al. (2013)), the error can be estimated as a maximum of 5%. In addition to this, the measured angles have an error of approximately $\pm$ 2.5°(which is half of smallest possible step-size).

For the error due to the source, the temporal and thermal stability of it needs to be taken into account, however, the data sheet providing with this information was not available.

As already mentioned before, the spectrometer has an error of maximum 1%.

The human error in this experiment is relatively large as the spectrometer needs to be manually pointed at the illuminated spot on the sample. However, great care was taken to perform these measurements and after again cross-checking with literature it is established that this measurement error should be no more than 7%.

All in all, based on the previously mentioned errors the total error in this experiment is estimated to be 8.7%. After normalisation, the error needs to be compensated for the division by a measurement that also contains an error, for that the following formula is used:

$$\epsilon_{\text{total}} = \sqrt{\epsilon_1^2 + \epsilon_2^2},$$

(13)

In which ϵ_1 and ϵ_2 are the relative errors from two independent measurements. Each time reflectance is given in a figure, these will be the equations used to calculate the error, which gives a relative error of 12%.

4 Results

This chapter discusses the results of the experimental investigation using the in-house goniometer (see section 3.3) and collimated source (see section 3.2). The samples examined were a Lambertian reflector with a reflectance of 98%, paper, photo paper and a mirror. Section 4.1, gives a first look at the total spectral-angular results, whereas section 4.2 details the angular reflectance data and section 4.3 discusses the spectral results by comparing them with the UV-VIS spectroscope measurements.

4.1 Spectro-angular results

For each of the four main samples, measurements are performed for four different angles of incidences, ranging from -5° (near normal incidence) to 55° with a step-size of 20°. The spectral-angular measurements are shown for each sample below for an angle of incidence equal to 15°. For the other angle of incidences the figures are given in Appendix B. The different results for the measurements on the samples are shown in figure 14 below:
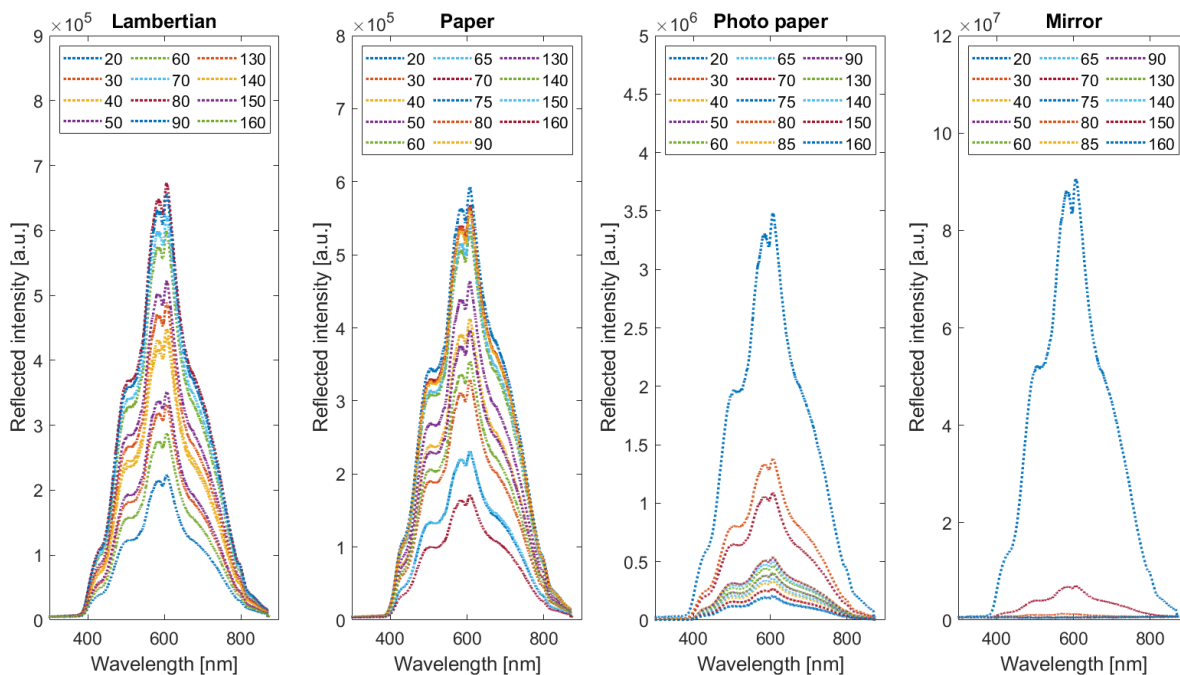

Figure 14: *Spectro-angular results on the reflected intensity for different angles on the goniometer for a Lambertian reflector, paper, photo paper and mirror. Angle of incidence is 15°.*

The graph above shows the high intensity for mirror around the angle of reflection (more than 100 times higher than the maximum measured intensity for the Lambertian reflector) and photo paper (approximately 10 times higher). Similarities between the paper and Lambertian measurements are also shown: both have a similar maximum reflected irradiance and for both this is around the surface normal. The further away from the surface normal, the lower the measured intensity is for both the paper and Lambertian sample. However, to fully define the spectro-angular albedo properties of the surfaces, these graphs were dissected into two parts: The first part shows the angular reflectance for a specific wavelength and the other part shows the spectral dependence of the reflectance of the samples. The results for the angular and specular reflectance are shown in the upcoming subsections.

4.2 Angular reflectance

In this section, the reflected intensity for different spots on the goniometer will be given for a wavelength of 550 nm. Similar behaviour is observed for different wavelengths, but only one is shown here to keep it concise.

The measurements for the perfect Lambertian are shown in figure 15. In this figure the effect of the Fresnel Term can be observed (see section 2.2.1 on page 11) as this term plays an increasingly large role for larger angles of incidences. Because of this, a larger portion of the light is specularly reflected around the angle of reflection, causing the fit to be of lower quality.

The data points were fitted to a cosine function, because the diffuse measured reflectance is expected to be cosine dependent (see equation 10), and the resulting function was used to generate the intensity profile for the entire hemisphere. This function was also used for the normalisation of each data point (see section 3.7).
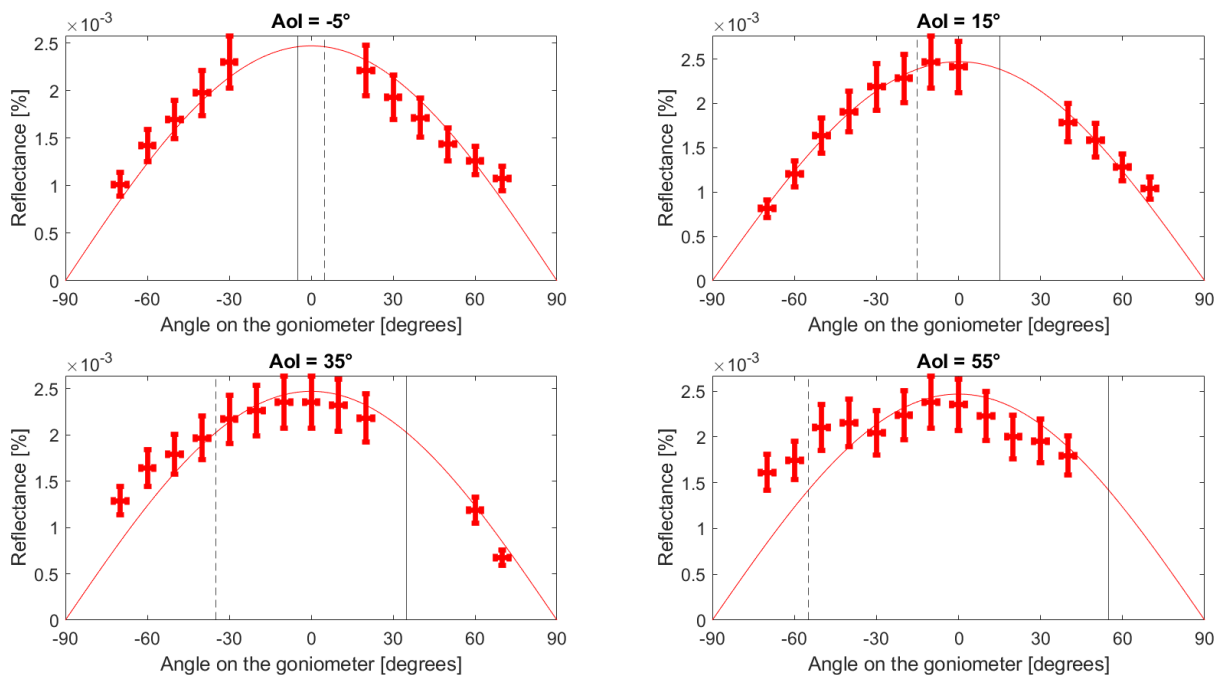

Figure 15: *Angular reflectance for paper for different angles on the goniometer. The angle of incidence (AoI) is shown in the black solid vertical line and angle of reflection is shown with a dashed vertical line.*

The measurements on paper are shown in figure 16. Data points used for the cosine fit are shown using blue markers, whereas black data points are not considered for the fit. This is because of small, but finite, glossiness of the sample.

The paper measurements show clear diffuse behavior for the smaller angles of incidences (good cosine behaviour). For the largest angle of incidence, no cosine fit could be made to the data (hence all the data points are black). One possible explanation for this is again the Fresnel term that was also observed at the Lambertian measurements. That the effect of the Fresnel term is stronger for paper then for the Lambertian can be explained by the fact that the Lambertian is designed to be a

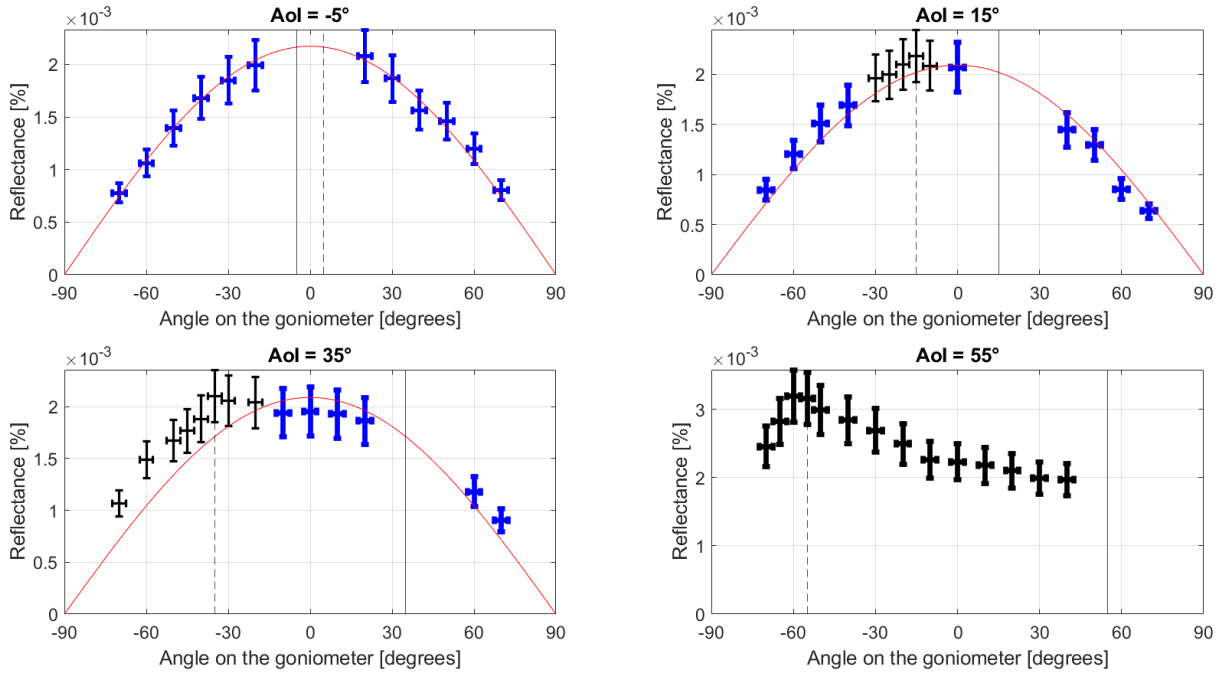high-quality reflector and for paper this is not the case.

Figure 16: *Angular reflectance for paper for different angles on the goniometer. The angle of incidence (AoI) is shown in the black solid vertical line and the angle of reflection is shown with a dashed vertical line. Cosine fits were made to the data, data points excluded from the fit are black.*

The measurements on photo paper are shown in figure 17. Again cosine fits were made to the data, excluding the points that are inside the glossy lobe. The measurements again show the influence of the Fresnel term as the glossy reflection part gets higher for larger angle of incidences. For the near normal incidence measurement, no lobe could be observed due to the self-shading of the fibre. Despite this, clear diffuse behaviour for angles not equal to angle of reflection was observed.

The measurements on the mirror are shown in figure 18. For the near normal incidence, no signal could be measured due to the self-shading of the fibre. No cosine fits could be made to this data, suggesting the absence of diffuse reflection, however a very narrow lobe around the angle of reflection (dashed line) can be observed for all three measurements. In a similar way as for the photo paper measurements, the Fresnel term can be observed in these plots as the maximum intensity of the peak gets higher for the larger angles of incidences.

4.3 Verification using UV-VIS spectroscopy

In this section, the cosine fits from the previous sections on paper and photo paper and the Lambertian measurements were used (using equation (11)) to get to total (diffuse) reflection over the hemisphere. This data is then compared to the data gathered by Shweta Pal with the UV-VIS measurements (see figure 19).
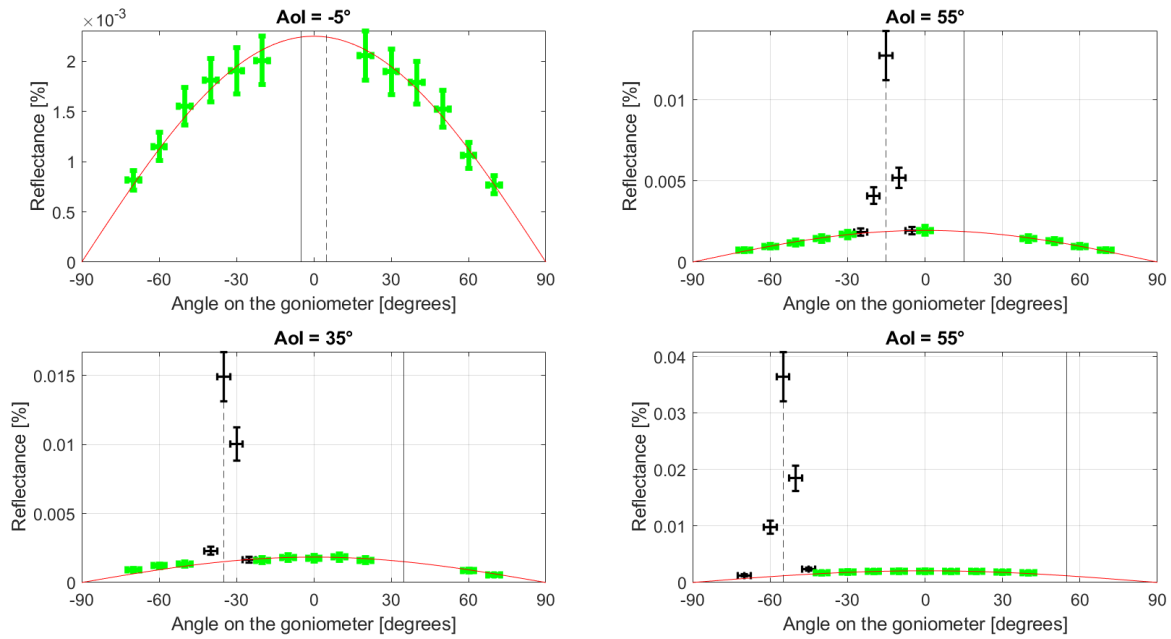
Figure 17: *Angular reflectance for photo paper for different angles on the goniometer. The angle of incidence (AoI) is shown in the black solid vertical line and the angle of incidence is shown with a dashed vertical line. Cosine fits were made to the data, data points excluded from the fit are black.*
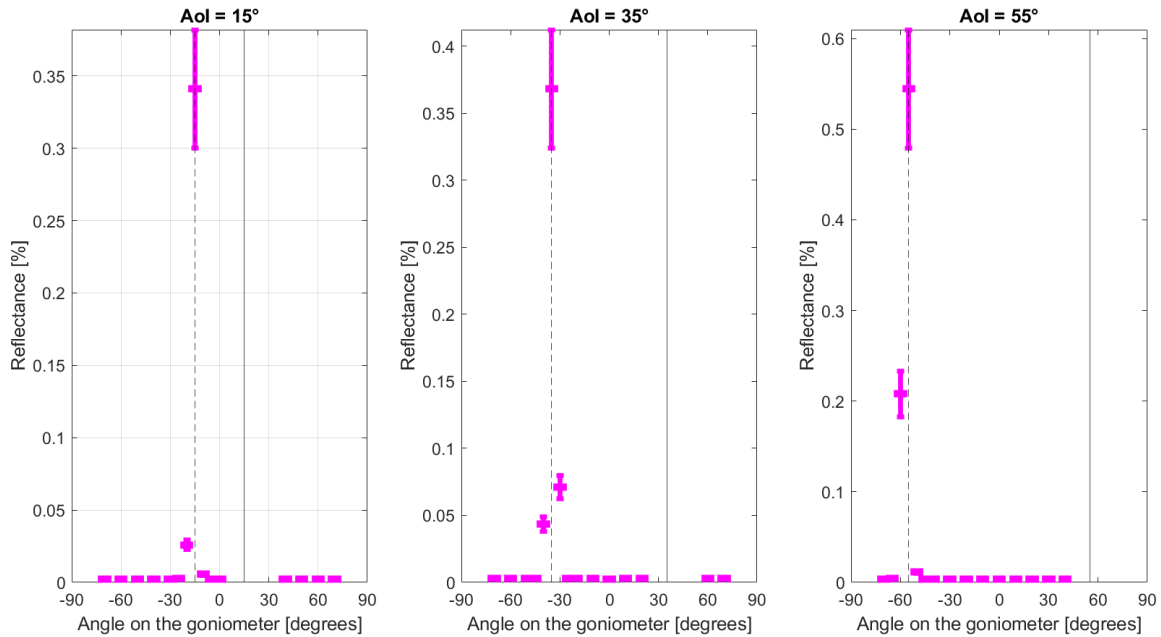

Figure 18: *Angular reflectance for mirror for different angles on the goniometer. The angle of incidence (AoI) is shown in the black solid vertical line and the angle of reflection is shown with a dashed vertical line.*
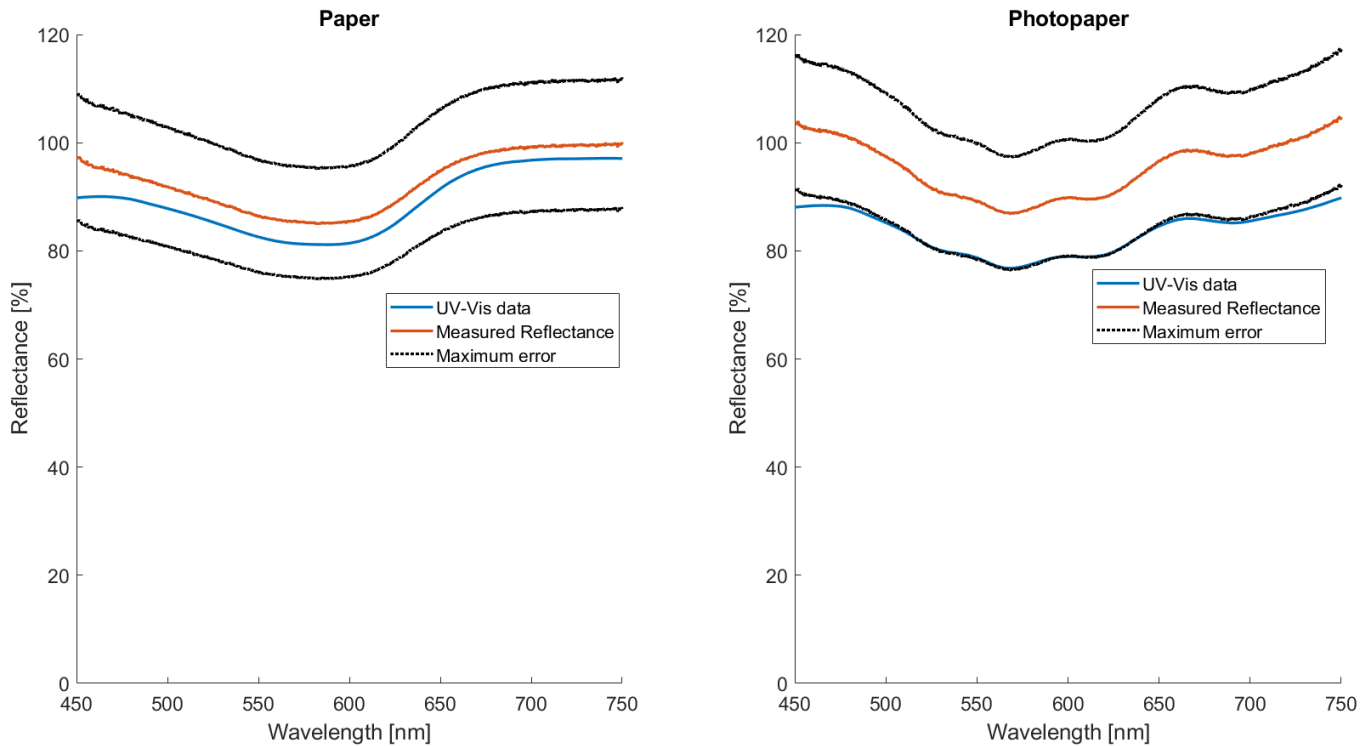
Figure 19: *Specular results gathered after integrating the acquired cosine fit over the hemisphere for both paper and photo paper. The maximum error for these measurements are shown in black. Compared to the UV-Vis data.*

From figure 19 we notice that the data acquired using the goniometer mimic the curves obtained using the UV-VIS for paper. Using this information, we extend our analysis to photo paper as well. The maximum difference between the paper reflectance acquired using the goniometer and the UV-VIS is 6% at the 450nm range and for photo paper it is slightly larger with 14%. Such an agreement between these two independent measurements serves as a confirmation in the reliability of the goniometer set-up for the scope of this study.

For photo paper, at the edges of the spectrum a reflection of higher then 100% intensity is measured, which is not what is expected. One possible explanation is that either the cosine fit on the photo paper measurement had a too large amplitude, or that the amplitude from the cosine fit on the Lambertian reflector was too low (or a combination of both). According to the error (given by the black lines) a possible curve exists where each point is below 100% reflectance. Another possible explanation can be derived from the fact that, often, both photo paper and paper contain whiteners that absorb light from a certain wavelength and emit it in another to make the surface more white. More on these whiteners is explained by Murray (1996). Technically, these whiteners could absorb one wavelength and emit another, causing the emitted wavelength to have a reflectance of higher than 100%.

The measurements on the paper sample are closer to the data of the UV-VIS than that is the case for the photo paper sample. For the measurements on the goniometer, layers of the sample were used to perfectly center it at the goniometer, for the UV-VIS measurement, initially, only one layer was used. It was observed that there was transmission through the paper and thus for the paper sample

the UV-VIS measurements were repeated with more layers of paper (that data is shown here for 8 layers). A similar thing happened for the photo paper, but the data for the UV-VIS was not repeated there, which explains that it is slightly lower than compared to the paper measurement. In the future, the measurements on the goniometer and on the UV-VIS should be compared for the same number of layers.

The spectral results for the mirror measurement were unobtainable. Due to the high sensitivity of the fibre's orientation and angular width of the reflected peak, a small measurement error would greatly change the fit and thus the measurement results. Besides, it becomes clear from the angular graphs that there is no diffuse behavior for the mirror sample so from equation (1) $k_s = 1$. For the Lambertian, no specular or glossy reflection could be observed so $k_d = 1$. The coefficients for paper and photo paper are still inconclusive as the reflectance that is measured is higher then the reflectance measured at the UV-VIS. This will be discussed more in-depth in the next chapter.

4.4   Ward fit

In the previous sections, diffuse reflection was modelled using a simple cosine fit. In an attempt to derive the surface parameters for glossy and specular reflection for the various samples, Ward's model (see section 2.2.5 and equation 10) was fitted onto the data for a paper, photo paper and mirror measurement (see figure 20).
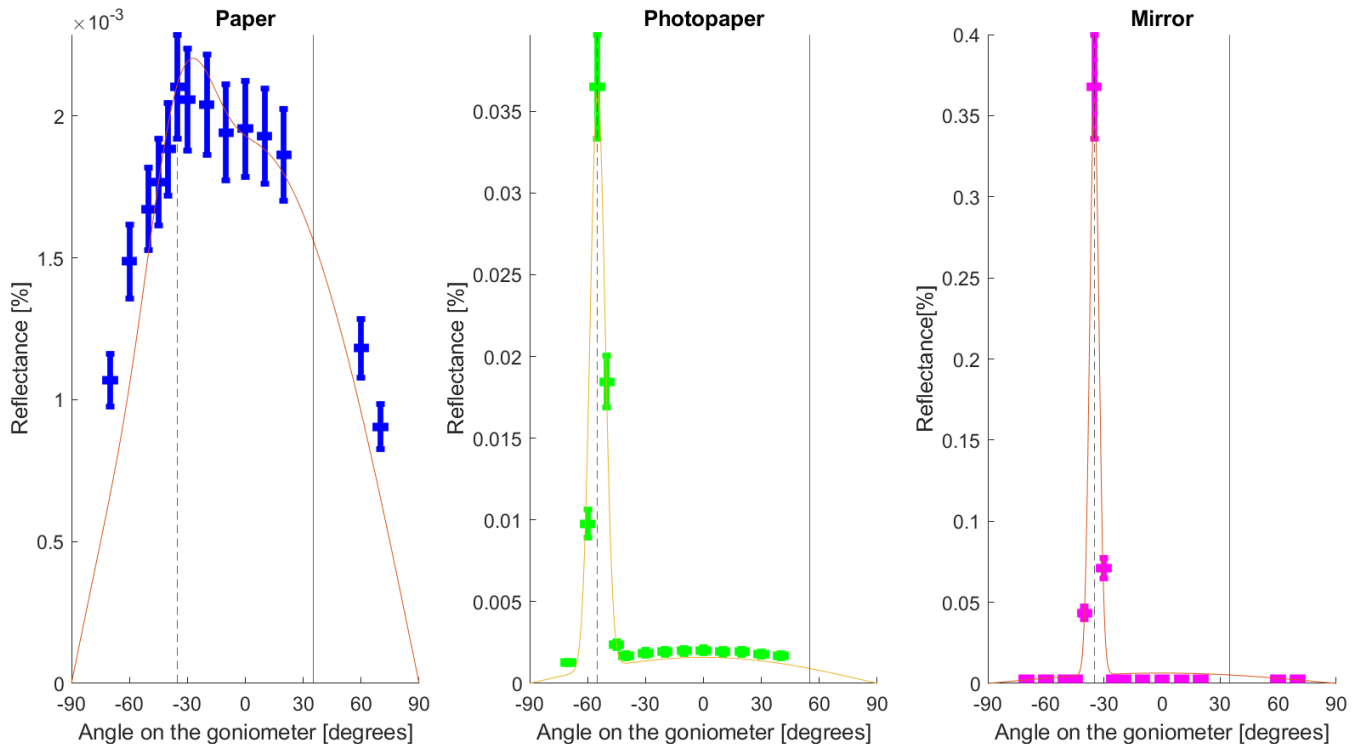

Figure 20: *Ward's model fitted over the data points for three different samples. The black solid vertical lines indicate the angle of incidence for each sample and the dashed line indicates where angle of reflection = angle of incidence.*

I made the fit in Matlab using a mean square approximation over the three parameters / three degrees

of freedom (σ, ρ_d, ρ_s). For the largely diffuse sample (paper) the fit is not as good, possibly due to the influence of the Fresnel term, as that is not taken into account by this model. For the other samples, however, the model is much more in agreement. For photo paper, the diffusive parameter might be a bit too low, and for mirror a bit too high, but the overall shape of the curve matches well, especially for the peaks. These peaks could be rotated around their axes to obtain a value for the intensity due to glossy and/or specular reflection. However, due to the sensitivity of the fibre's orientation and the small angular width of the reflected peak, a small measurement error would greatly change the fit and thus the measurement results. Besides this, no diffuse reflectance could be observed for the mirror measurement so for that this would not be necessary.

This chapter showed the results of all the measurements: For the angular reflectance of samples, cosine fits were made to model the diffuse reflectance of the samples, and Ward's model was used to gain more insight into the specular and glossy reflectance of the samples. In addition to this, the experiments validity was confirmed in a comparison between two independent spectral reflectance measurements, one with the in-house goniometer set-up and one with a UV-VIS spectroscope (measurements on the spectroscope were performed by Shweta Pal).

The expectations that paper, photo paper and mirror are each extreme cases of their corresponding type of reflection were correct for the lambertian and the mirror. For the photo paper, diffuse behaviour could clearly be observed in addition to the glossy reflection and curves were made to fit this diffuse behaviour (see figure 17). In addition to the surface integral of the diffusive part over the hemisphere, the glossy part could be rotated around the axis of angle of reflection (black dashed line in the figures). To do this, a function defining the glossy reflection would need to be fit onto the data. A first attempt for this is made using Ward's model. The ratio between these two integrals would then give the coefficients for glossy and diffuse reflection, however due to the sensitivity of set-up the validity of the glossiness peak could not be confirmed at this time.

5   Conclusion & Discussion

In this study, the albedo properties of various surfaces are experimentally defined using an in-house goniometer that was designed for this study. It was expected that each of these sample surfaces are extremes of one of the types of reflection: Lambertian and paper are expected to be diffuse, mirror is expected to be specular, and photo paper is expected to be glossy. These expectations were correct for the Lambertian and the mirror (giving k_d equals 1 for the Lambertian and k_s equals 1 for the mirror. For the photo paper, diffuse behaviour could clearly be observed in addition to the glossy reflection and curves were made to fit this data (see figure 17). In addition to the surface integral of the diffusive part over hemisphere, the glossy part could be rotated around the angle of reflection axis (black dashed line in the figures). To do this, a function defining the glossy reflection would need to be fit onto the data. A first attempt for this is made using Ward's model. The ratio between these two integrals would then give the coefficients for glossy and diffuse reflection.

For paper, the case is more complex, as there is also a small glossy term and the Fresnel term (see section 2.2.1 largely influences the data. Future work could fit the data to the more rigorous GGX model that also includes the influence of the Fresnel term. For the GGX model, see Walter et al. (2007).

The shape of the spectral results are in accordance with the data gathered from the UV-VIS. One of the improvements would be to redo the experiments with a calibrated spectrometer, to check the validity of the normalisation terms and get a better grasp on the total reflectance of a sample. In addition to this, the used spectrometer worked in the 200-850nm range, but the lightsource had a larger spectrum (up to approximately 900 nm, see figure 8), causing some of the light to be lost from the beginning.

To reduce measurement (human) errors, the setup could be automated. Doing this would also open up the possibility of performing continuous measurements instead of measurements with a 5° increment. Partly, due to a missing cosine corrector, the measurement errors for these experiments are relatively large. Despite this, important conclusions can still be drawn from the gathered data.

Future studies could perform measurements on a wider variety of samples, including more exotic samples for which azimuthal symmetry can not be assumed. For this to be possible, the 2D setup would need to be transformed to a 3D one. In addition to this, the actual influence of the albedo of the surfaces on the output of bifacial cells could be checked.

The data gathered in this study can be used to validate the raytracing that is done by Pal and Saive (2020) or by others that perform similar studies. Others can use this data as input for their ray-tracing software to calculate PV-output. When the albedo is properly defined, the LCOE for bifacial PV becomes lower, thus making them more economically attractive. The ray-tracing software can, using a linear combination of the three classes of reflectors assessed here as input, provide the optimum module-reflector configuration for a given location. Next to this, it can also assess the performance of reflectors that are presently underneath bifacial solar cells such as concrete or grass. Together with the data gathered here, the software can provide a thorough understanding of the spectro-angular albedo properties of various materials and it can thus be used to design exotic materials with ideal albedo properties.

6 References

Bisquert, J. (2008). The two sides of solar energy. *Nature Photonics*, 2(11):648–649.

Cook, R. L. and Torrance, K. E. (1981). A reflectance model for computer graphics. *ACM Siggraph Computer Graphics*, 15(3):307–316.

Cuevas, A., Luque, A., Eguren, J., and del Alamo, J. (1982). 50 per cent more output power from an albedo-collecting flat panel using bifacial solar cells. *Solar Energy*, 29(5):419–420.

Dullweber, T., Schulte-Huxel, H., Blankemeyer, S., Hannebauer, H., Schimanke, S., Baumann, U., Witteck, R., Peibst, R., Köntges, M., Brendel, R., et al. (2018). Present status and future perspectives of bifacial perc+ solar cells and modules. *Japanese Journal of Applied Physics*, 57(8S3):08RA01.

EIA (2020). Annual energy outlook 2020. *Energy Information Administration, Washington, DC*.

Einhaus, L. and Saive, R. (2020). Free-space concentration of diffused light for photovoltaics. In *2020 47th IEEE Photovoltaic Specialists Conference (PVSC)*, pages 1368–1370. IEEE.

Feldman, D. and Margolis, R. (2020). Q4 2019/q1 2020 solar industry update. Technical report, National Renewable Energy Lab.(NREL), Golden, CO (United States).

Fertig, F., Nold, S., Wöhrle, N., Greulich, J., Hädrich, I., Krauß, K., Mittag, M., Biro, D., Rein, S., and Preu, R. (2016). Economic feasibility of bifacial silicon solar cells. *Progress in photovoltaics: research and applications*, 24(6):800–817.

Gambone, S. (2020). What are bifacial solar panels.

Georgiev, G. T. and Butler, J. J. (2007). Long-term calibration monitoring of spectralon diffusers brdf in the air-ultraviolet. *Applied Optics*, 46(32):7892–7899.

Hecht, E. (2017). *Optics*. Pearson Education India, 5 edition.

Hezel, R. (2003). Novel applications of bifacial solar cells. *Progress in Photovoltaics: Research and Applications*, 11(8):549–556.

IEA (2020a). Global energy review 2019.

IEA (2020b). Global energy review 2020.

Ito, M. and Gerritsen, E. (2016). Geographical mapping of the performance of vertically installed bifacial modules. In *32nd European Photovoltaic Solar Energy Conference and Exhibition*, pages 1603–1609.

Katsaounis, T., Kotsovos, K., Gereige, I., Basaheeh, A., Abdullah, M., Khayat, A., Al-Habshi, E., Al-Saggaf, A., and Tzavaras, A. (2019). Performance assessment of bifacial c-si pv modules through device simulations and outdoor measurements. *Renewable Energy*, 143:1285–1298.

Kopecek, R. and Libal, J. (2018). Towards large-scale deployment of bifacial photovoltaics. *Nature Energy*, 3(6):443–446.

Lambert, J. H. (1760). *Photometria sive de mensura et gradibus luminis, colorum et umbrae*. sumptibus vidvae E. Klett, typis CP Detleffsen.

Libal, J., Berrian, D., and Kopecek, R. (2017). Overview: energy yield simulations and calculation of lcoe for bifacial pv systems. *Bifi PV Work*.

Love, R. C. (1997). *Surface reflection model estimation from naturally illuminated image sequences*. PhD thesis, University of Leeds.

Mardaljevic, J. (1995). Validation of a lighting simulation program under real sky conditions. *International Journal of Lighting Research and Technology*, 27(4):181–188.

Murray, S. (1996). Dyes and fluorescent whitening agents for paper. In *Paper Chemistry*, pages 161–193. Springer.

Nelson, J. A. (2003). *The physics of solar cells*. World Scientific Publishing Company.

Nicodemus, F. E. (1965). Directional reflectance and emissivity of an opaque surface. *Applied optics*, 4(7):767–775.

Nicodemus, F. E., Richmond, J. C., Hsia, J. J., Ginsberg, I., and Limperis, T. (1992). Geometrical considerations and nomenclature for reflectance. *NBS monograph*, 160:4.

Paidipati, J., Frantzis, L., Sawyer, H., and Kurrasch, A. (2008). Rooftop photovoltaics market penetration scenarios. Technical report, National Renewable Energy Lab.(NREL), Golden, CO (United States).

Pal, S. and Saive, R. (2020). Output enhancement of bifacial solar modules under diffuse and specular albedo.

Pelaez, S. A., Tan, S. X., Chrysler, B., Zhao, J., Wu, Y., and Kostuk, R. K. (2018). Holographic cap collectors for enhanced mid-day energy production of vertically mounted bifacial photovoltaic modules. In *Nonimaging Optics: Efficient Design for Illumination and Solar Concentration XV*, volume 10758, page 107580P. International Society for Optics and Photonics.

Phillips, A. B., Subedi, K. K., Liyanage, G. K., Alfadhili, F. K., Ellingson, R. J., and Heben, M. J. (2020). Understanding and advancing bifacial thin film solar cells. *ACS Applied Energy Materials*, 3(7):6072–6078.

Porter, W. (2019). Bifacial modules: There are two sides to every solar panel. Technical report, Burns McDonnel.

Rodríguez-Gallegos, C. D., Bieri, M., Gandhi, O., Singh, J. P., Reindl, T., and Panda, S. (2018). Monofacial vs bifacial si-based pv modules: Which one is more cost-effective? *Solar Energy*, 176:412–438.

Russell, T. C., Saive, R., and Atwater, H. A. (2017). Thermodynamic efficiency limit of bifacial solar cells for various spectral albedos. In *2017 IEEE 44th Photovoltaic Specialist Conference (PVSC)*, pages 1531–1536. IEEE.

Sampaio, P. G. V. and González, M. O. A. (2017). Photovoltaic solar energy: Conceptual framework. *Renewable and Sustainable Energy Reviews*, 74:590–601.

Solar Magazine (2020). Bifacial solar panels: Residential use and trends.

Sun, X., Khan, M. R., Deline, C., and Alam, M. A. (2018). Optimization and performance of bifacial solar modules: A global perspective. *Applied energy*, 212:1601–1610.

Taibi, E., Nikolakakis, T., Gutierrez, L., Fernandez del Valle, C., Kiviluoma, J., Lindroos, T., and Rissanen, S. (2018). Power system flexibility for the energy transition.

Thorlabs (2021). Integrating spheres.

VDMA (2020). International Technology Roadmap for Photovoltaic (ITRPV), 2019 results.

Viral International (2014). Reflectance models.

Walter, B., Marschner, S. R., Li, H., and Torrance, K. E. (2007). Microfacet models for refraction through rough surfaces. *Rendering techniques*, 2007:18th.

Wang, H., Zhang, W., and Dong, A. (2013). Measurement and modeling of bidirectional reflectance distribution function (brdf) on material surface. *Measurement*, 46(9):3654–3661.

Ward, G. J. (1992). Measuring and modeling anisotropic reflection. In *Proceedings of the 19th annual conference on Computer graphics and interactive techniques*, pages 265–272.

Xu, Y., Zhang, J., Xuan, Y., Wang, J., and Meng, F. (2020). Synergetic or colliding effects on the solar-electric conversion efficiency from light-trapping structured surfaces: Coupling optical-electrical features of bifacial solar cells. *Solar Energy*, 207:517–527.

Yusufoglu, U. A., Pletzer, T. M., Koduvelikulathu, L. J., Comparotto, C., Kopecek, R., and Kurz, H. (2015). Analysis of the annual performance of bifacial modules and optimization methods. *IEEE Journal of Photovoltaics*, 5(1):320–328.

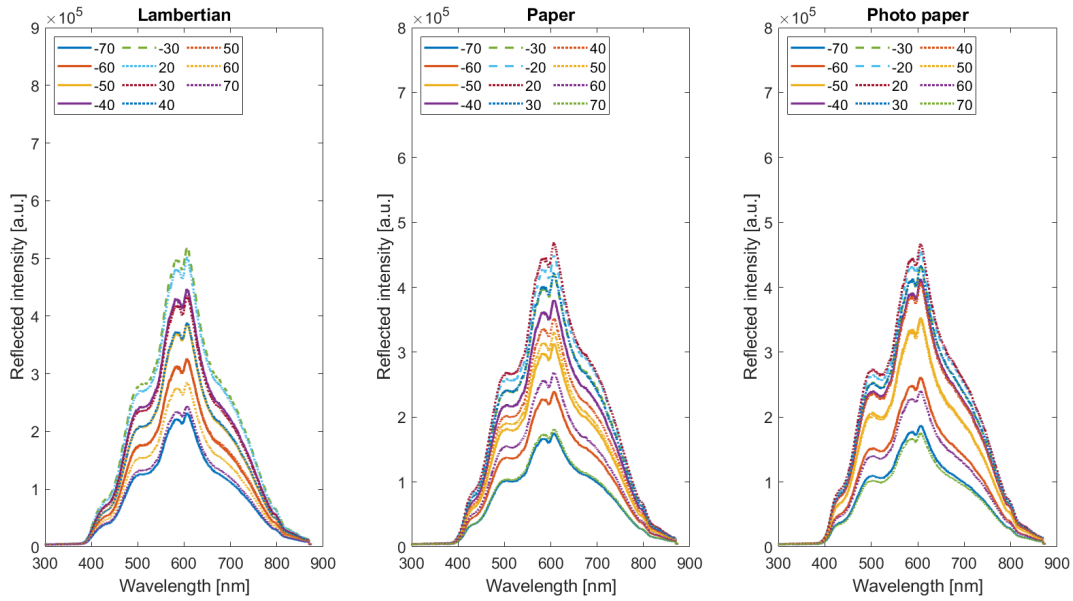# A   Lasercut-file
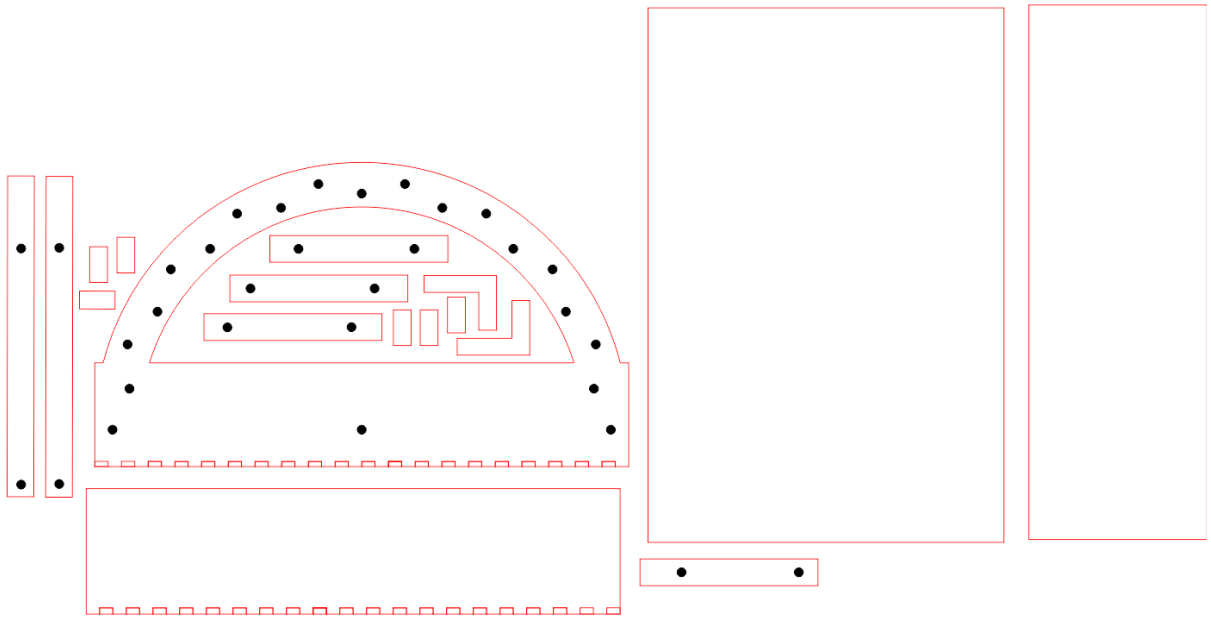
B Spectro-angular plots

Figure 21: *Spectro-angular results on the reflected intensity for different angles on the goniometer for a Lambertian reflector, paper, photopaper and mirror. Angle of incidence is -5°*
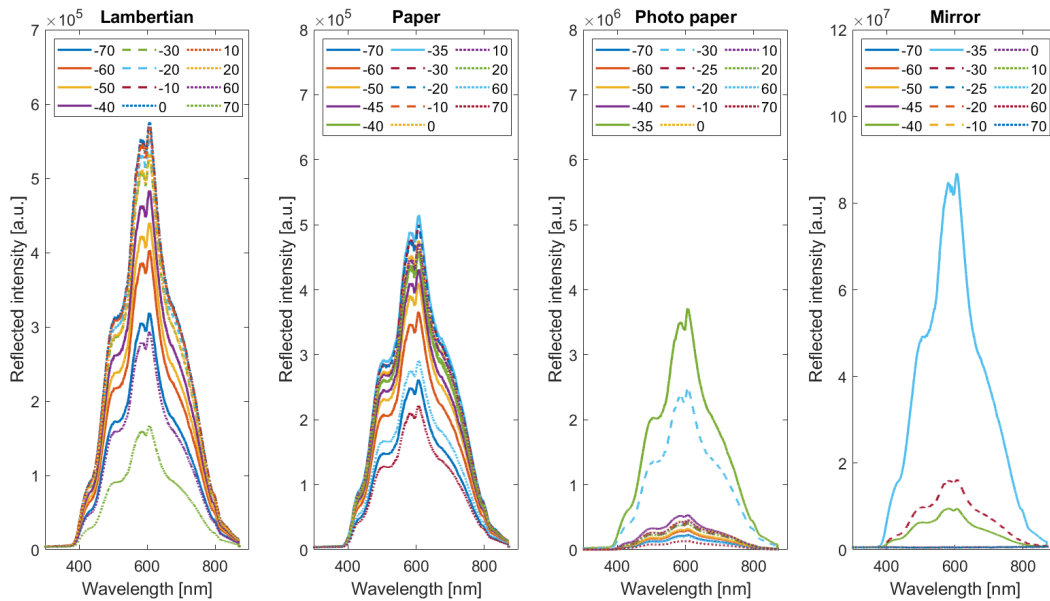

Figure 22: *Spectro-angular results on the reflected intensity for different angles on the goniometer for a Lambertian reflector, paper, photopaper and mirror. Angle of incidence is 35°*
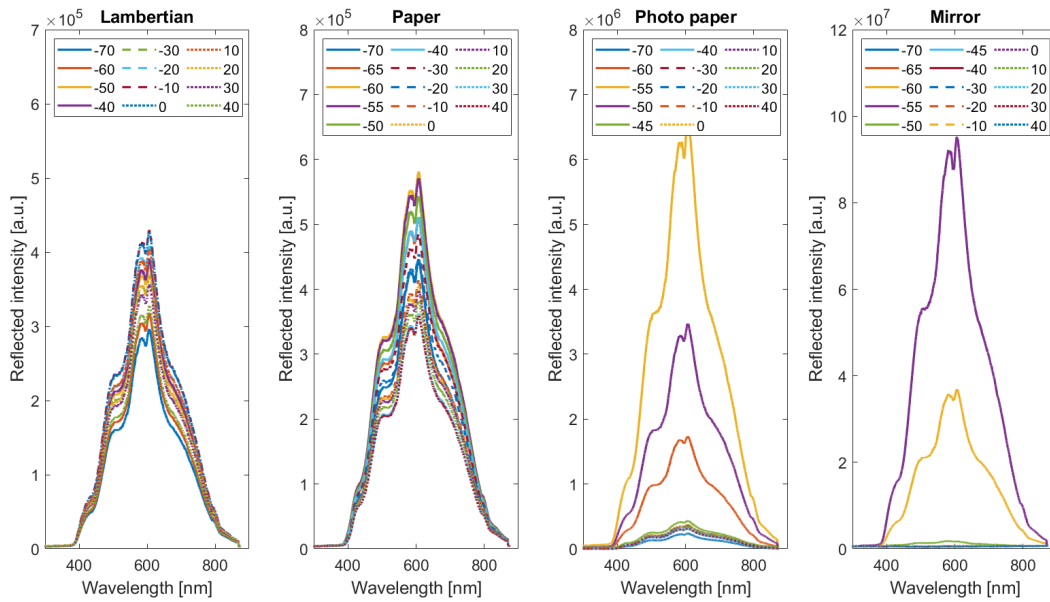
Figure 23: *Spectro-angular results on the reflected intensity for different angles on the goniometer for a Lambertian reflector, paper, photopaper and mirror. Angle of incidence is 55°*